https://doi.org/10.5194/essd-2026-530
Preprint. Discussion started: 12 August 2026

Open Access Earth System Science Data Discussions

4-D Aviation Emission Inventory Data of China Estimated with QAR Data in 2023 (4D-AEID-2023)

Binbin Lu[1], Lingkun Shi[1], Chun Wang[2*], Huabo Sun[2], Qinli Guo[3], Xinbo Wang[3], Xuhui Wang[2*]

[1]School of Remote Sensing and Information Engineering, Wuhan University, Wuhan 430079, China
[2]China Academy of Civil Aviation Science and Technology, Beijing, 100028, China
[3]Capital Airports Holdings Co., Ltd. Beijing Construction Project Management Headquarters, Beijing, 100028, China

Correspondence to: Chun Wang (wangchun@castc.org.cn); Xuhui Wang (wangxh@castc.org.cn)

Abstract. Accurate aviation emission inventories are essential for environmental impact assessment and mitigation, yet existing estimates predominantly rely on aircraft performance models and standardized assumptions, introducing significant uncertainties. Here, we present a high-resolution, four-dimensional aviation emission inventory for China's civil aviation sector in 2023, built directly from Quick Access Recorder (QAR) data covering 4.52 million flights (~96.8% of national commercial movements). By coupling second-level fuel-flow measurements with observed flight-state and meteorological parameters via the Boeing Fuel Flow Method 2 and a dynamic thermodynamic correction, this dataset yields temporally and spatially explicit emission estimates for CO_2, NO_x, SO_2, PM, CO, and HC across all flight phases. In 2023, China's civil aviation consumed 28.4 Mt of fuel, emitting 89.3 Mt CO_2, 634.6 kt NO_x, 28.4 kt SO_2, 8.46 kt PM, 44.3 kt CO, and 6.35 kt HC. Monte Carlo analysis demonstrates that direct physical observations substantially constrain inventory uncertainty, reducing coefficients of variation (CV) for major pollutants to 2%–10% and shifting the dominant error source from activity-level assumptions to emission index parameterizations. High temporal resolution reveals pronounced phase-specific variations: taxiing accounts for 23.7% of HC and 19.4% of CO emissions due to low-thrust incomplete combustion, while the brief high-thrust acceleration segment preceding climb contributes 18.0% of total PM. Spatially, emissions are highly concentrated, with the top 10% of grid cells accounting for 74.2% of national CO_2 emissions, exhibiting significant clustering (Global Moran's I = 0.3389, $p < 0.05$) along major corridors. Providing second-level and high resolution, this dataset serves as an observation-based benchmark for refining existing inventories and assessing near-airport air quality. The dataset is publicly available at https://doi.org/10.5281/zenodo.20828076 (Lu et al., 2026).

1 Introduction

The robust recovery of aviation demand has positioned the air transport industry as a key driver of economic development in the post-pandemic era. However, its expanding environmental footprint presents a formidable challenge to achieving global carbon neutrality goals (Grewe et al., 2021; Johansson et al., 2025). Aircraft engines release a variety of emissions, including carbon dioxide (CO_2), nitrogen oxides (NO_x), carbon monoxide (CO), and non-volatile particulate matter (nvPM). These emissions may alter the Earth's radiation balance through the greenhouse effect and contrail cirrus (Schumann et al., 2012),

https://doi.org/10.5194/essd-2026-530
Preprint. Discussion started: 12 August 2026

significantly contributing to anthropogenic radiative forcing and climate change (Dannet et al., 2025; Lee et al., 2021). Furthermore, they may pose serious threats to public health by deteriorating regional air quality (Yim et al., 2013). Statistics indicate that global aviation emissions at cruise altitudes cause approximately 8,000 to 58,000 premature deaths annually, accounting for roughly 1% of global premature deaths attributed to air quality issues (Barrett et al., 2010). Given its spatio-temporally heterogeneous features, accurate quantification of aviation emission inventory is essential. Clarifying their complex distributions serves as the scientific foundation for effective emission control and comprehensive environmental impact assessment (Lu et al. 2024).

High-resolution aviation emission inventory serves as a critical link connecting aviation activities with atmospheric environmental responses. They provide precise inputs for climate and air quality models. Consequently, the data quality of these inventories directly determines the reliability of environmental models and emission reduction strategies (Simone et al., 2013; Stettler et al., 2013). Inventory compilation methods have evolved from coarse-scale estimation to fine-grained characterization, generally categorized into top-down and bottom-up approaches. The top-down method primarily estimates emissions based on global or regional jet fuel sales statistics (e.g., from the IEA). While computationally simple, this method is limited by spatiotemporal aggregation and usually fails to provide high-resolution spatial distribution information. In contrast, the bottom-up method estimates fuel consumption and emissions by aggregating individual flight data. The latter approach significantly enhances inventory precision and resolution (Cui et al., 2022).

Nevertheless, conventional bottom-up models typically rely on simplified assumptions by presuming that flights follow ideal great circle (GC) routes and adopt optimal cruise altitude and speed profiles (European Environment Agency., 2023; Wilkerson et al., 2010a). This idealization usually overlooks horizontal and vertical trajectory deviations in real-world flights caused by airspace control, meteorological conditions, and flight conflict. Such simplifications lead to a systematic underestimation of flight distance, fuel consumption, and emissions (Seymour et al., 2020; Tian et al., 2020). Studies show that estimates based on GC routes may underestimate flight distance by approximately 5% - 9% and omit about 20% - 25% of NO_x emissions (Yang et al., 2018).

In recent years, the proliferation of Automatic Dependent Surveillance-Broadcast (ADS-B) technology has facilitated a shift from grid-level to trajectory-level inventories. ADS-B provides high-frequency three-dimensional position information. This enables the precise resolution of track deviations, altitude changes, and phase durations, thereby improving the spatiotemporal resolution of activity data (Teoh et al., 2024). However, ADS-B records only kinematic variables such as position and speed. It lacks essential environmental parameters and fuel flow (FF) data (Zhao et al., 2024). Consequently, existing ADS-B-based studies still rely on generic aircraft performance models (e.g., BADA) combined with meteorological reanalysis data (Brandon Graver et al., 2019; ICAO, 2017; Nuic et al., 2010). Although this 'trajectory + model' approach adds four-dimensional information, they generally struggle to capture individual aircraft performance differences and instantaneous operational fluctuations. This leads to persistent systematic biases between estimated and actual fuel consumption (Quadros et al., 2022; Teoh et al., 2024; X. Zhang et al., 2019). Uncertainties are particularly pronounced during the high-altitude cruise phase when quantifying NO_x and nvPM emissions, as these are highly sensitive to combustion conditions (Kim et al., 2007). Therefore, incorporating airborne observations to characterize engine operating states is crucial. Developing an observation-constrained four-dimensional emission inventory is a critical challenge for reducing estimation uncertainties.(J. Wang et al., 2024).

Quick Access Recorder (QAR) data has been widely regarded as the source with the highest physical fidelity for flight operations quality assurance and emission estimation (L. Wang et al., 2014; Dong et al., 2022). It directly records a variety of aircraft avionics data, including fuel flow, N1/N2 rotational speeds, exhaust gas temperature, pressure altitude, and ambient temperature. QAR data captures transient thrust fluctuations caused by pilot operations (Koudis et al., 2017) and performance degradation due to engine model differences (Abrahamson et al., 2016). This capability eliminates dependence on generic performance models, realizing a transition from model-parameterized estimation to the use of measured flight operational parameters. Current public research mostly focuses on short-term samples from single routes or airports, lacking systematic analysis at the national scale (Ma et al., 2024a; Xu et al., 2020). Consequently, the potential of QAR data to correct biases in macroscopic inventories has not yet been fully exploited.

To address these limitations, this study constructs a national-scale aviation emission inventory for China's civil aviation sector using QAR records from approximately 4.52 million flights operated in 2023. By coupling measured fuel flow with airborne thermodynamic parameters, we derive a high-resolution, four-dimensional inventory of CO_2, NO_x, SO_2, PM, CO, and HC emissions, and quantify how estimation uncertainty, and its dominant sources which differ from conventional, model-based approaches. This observation-based framework addresses the absence of large-scale, real-world measurement in existing national inventories, reveals systematic biases in performance-model-based estimates under complex operating conditions, and provides a basis for evaluating and refining the aviation emission products currently used in policy and air-quality assessment.

2 Methodology and Data

2.1 Research Framework

Figure 1 presents the technical framework of this study, comprising three sequential stages. The first stage integrates multi-source data: high-frequency QAR records (1 Hz fuel flow and ambient parameters from 4.52 million flights in 2023), flight schedule metadata, and the ICAO Engine Emissions Databank (EEDB). Based on these three data sources, the second stage implements an engine-specific emission modeling pipeline. Aircraft in the fleet are first matched to their specific engine types to identify the corresponding reference Emission Index (EI) curves; baseline EIs are then derived from real-time single-engine fuel flow. To account for real-world thermodynamic variations, the baseline EIs are corrected for ambient conditions using the Boeing Fuel Flow Method 2 (BFFM2), driven directly by airborne-measured environmental parameters. The corrected EIs are multiplied by instantaneous fuel flow to obtain second-resolution emission rates(DuBois & Paynter, 2006; Yoder, 2007), which are aggregated across the fleet in space and time to produce a high-resolution, four-dimensional aviation emission inventory. In the third stage, the inventory is evaluated along four dimensions: overall characteristics, uncertainty, spatial structure, and temporal patterns.

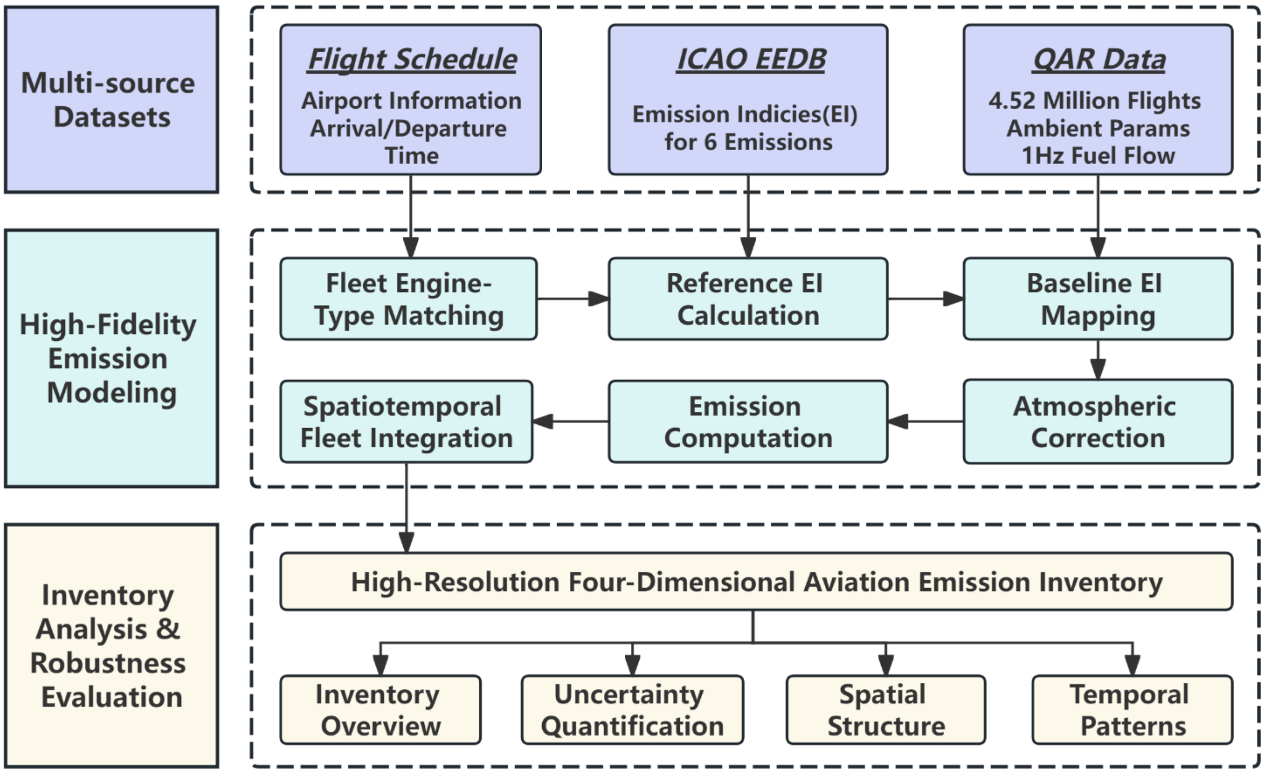

Figure 1: Technical framework of this study, including three stages: data fusion, core calculation models, and inventory analysis.

2.2 Data Description

2.2.1 QAR Data

The data foundation of this study stems from a massive airborne QAR dataset provided by the Civil Aviation Flight Quality Monitoring Base Station of China. This dataset covers approximately 4.52 million flights operating to and from civil airports across China throughout 2023.The QAR data contains over 2,000 parameters throughout the full flight at a frequency of 1 Hz recorded via the airborne Flight Data Acquisition Unit (FDAU) (Dong et al., 2022). Beyond latitude, longitude, and altitude, the QAR data fully covers key thermodynamic parameters such as Fuel Flow (FF), engine rotational speeds (N1/N2), and Exhaust Gas Temperature (EGT). Moreover, it captures real-world environmental parameters, including static air temperature, static pressure, and wind speed (Table 1). Compared to studies relying on generic performance models like BADA, the direct use of airborne measured parameters significantly reduces fuel estimation biases caused by idealized assumptions (Wilkerson et al., 2010b; Yanto & Liem, 2018).

Table 1: QAR Data Field Information

Field Name	Parameter Description	Unit	Interval (s)
FLIGHT_INFO_ID	Flight Sequence Number	-	-
FLIGHT_PHASE	Flight Phase	-	1
GPS_LAT_CA	Latitude	°	1
GPS_LONG_CA	Longitude	°	1
ALT_STDC	Corrected Standard Pressure Altitude	feet	1
FF1	Fuel Flow of Engine No. 1	lb/h	1
FF2	Fuel Flow of Engine No. 2	lb/h	1
SAT	Static Air Temperature	℃	1
IAS	Indicated Airspeed	kt	1
GS	Ground Speed	kt	1
WIN_SPD	Wind Speed	kt	1
IVV	Instantaneous Vertical Velocity	ft/min	1

The raw QAR archive used in this study spans 4.52 million flights recorded in 2023, sampled at 1 Hz across the full flight duration. As with any large-scale operational dataset accumulated across a heterogeneous fleet, the raw records are affected by sensor drift, transmission errors, and intermittent signal loss, and different aircraft types and recording systems introduce further inconsistencies in parameter naming and sampling continuity. Rather than assuming a uniform level of data quality across the archive, we therefore applied a staged reconstruction and cleaning procedure prior to any emission calculation.

Records were first screened for physical and logical consistency: flights with missing or invalid measurements in key variables (fuel flow, pressure altitude) were flagged, along with observations exhibiting values outside physically plausible ranges (e.g., negative fuel flow, altitude discontinuities inconsistent with vertical speed) or internal logical contradictions between correlated parameters(Gariel et al., 2011). This screening removed 1.6% of the original records from the archive, which were excluded from subsequent processing. Among the retained flights, most data quality issues took the form of short, isolated gaps rather than sustained loss of signal. For gaps shorter than 60 s, we applied linear interpolation to reconstruct second-level time series. This is justified by the physical continuity of aircraft motion and engine state: over such short intervals, abrupt discontinuities in speed, altitude, or fuel flow are not physically expected, so linear interpolation introduces negligible distortion while preserving trajectory continuity for downstream emission calculation.

A smaller subset of flights exhibited more extensive data loss, e.g., prolonged GPS outages or extended gaps in fuel flow or altitude, for which interpolation would no longer be reliable. For these cases, we adopted a similarity-based reconstruction:

https://doi.org/10.5194/essd-2026-530
Preprint. Discussion started: 12 August 2026

complete historical trajectories sharing the same route, aircraft type, and operational period were retrieved from the QAR archive and used as reference profiles for reconstruction. This step was intended to retain otherwise representative flights that would be lost under a stricter exclusion criterion, and thereby reduce the sampling bias that would result from systematically discarding flights with partial data loss.

To support subsequent phase-resolved emission calculation, the FLIGHT_PHASE field was mapped to numerical codes following the flight phase classification standard of the China Academy of Civil Aviation Science and Technology (CAST). Because FLIGHT_PHASE labels can be imprecise near phase transitions, we cross-validated the segmentation using auxiliary kinematic parameters, including Ground Speed (GS), Indicated Airspeed (IAS), and Inertial Vertical Velocity (IVV), to correct boundary misclassification. This yielded 12 flight phases representing a nominal flight profile; phase definitions are provided in Table S1, and the corresponding baseline altitude trends are shown in Figure S1.

2.2.2 Flight Schedule Data

Given that the aircraft type identifiers in raw QAR records utilize proprietary internal codes, this study incorporated an external flight schedule database to retrieve critical metadata, including airport pairs, standardized aircraft type designations, and, crucially, specific engine models. We compiled a comprehensive dataset of civil aviation operations in mainland China for the full year of 2023. This dataset encompasses core fields such as airline codes, flight numbers, four-letter ICAO airport codes, scheduled/actual timestamps, and aircraft registration numbers (Table 2).

Table 2: Basic Flight Field Information

Parameter	Parameter Description
FLIGHT_NO	Flight Number
AC_AIRLINE	Airline company
AC_TAIL	Aircraft tail number
AC_TYPE	Aircraft type
ENGTYPE	Engine type
LANDING_DATE	Landing date
TAKEOFF_DATE	Takeoff date
LANDING_TIME	Landing time
TAKEOFF_TIME	Takeoff time
ARRAP	Arrival airport
DEPAP	Departure airport

Prior to data fusion, strict quality control and standardization protocols were implemented. All temporal attributes were calibrated from Coordinated Universal Time (UTC) to China Standard Time (UTC+8) to align with national operational

https://doi.org/10.5194/essd-2026-530
Preprint. Discussion started: 12 August 2026

statistical standards. We employed a business logic-based repair and exclusion strategy to address anomalies such as null timestamps (e.g., 00:00:00), missing key fields, and character encoding errors. Invalid records containing logical paradoxes were thoroughly removed to ensure data integrity.

The cleaned flight schedule data were then linked to QAR trajectory records using the aircraft registration number as the unique identifier. This linkage enabled the precise assignment of specific engine models (e.g., distinguishing between different thrust ratings within the same engine family) to individual flights, effectively resolving the ambiguity often associated with generic fleet matching. The resulting fused dataset integrates fundamental flight attributes, dynamic operational states, and external environmental parameters. This integration provides a robust basis for analyzing the macroscopic spatiotemporal characteristics of China's air transport network and supports subsequent multidimensional, high-fidelity analyses of aviation emissions.

2.2.3 ICAO Emission Factor Database

This study adopted the ICAO Engine Emissions Databank (EEDB v31) (EASA, 2025) as the baseline data source for emission calculations. For each engine model identified in the QAR dataset, we established a dedicated emission index mapping table, directly extracting reference Emission Indices (EIs) for NO_x, CO, HC, and nvPM at four standard thrust settings (7%, 30%, 85%, and 100%). For CO_2 and SO_2, which are excluded from the EEDB, emissions were calculated based on the carbon and sulfur content of the fuel using the Mass Balance Principle. To overcome the limitation that EEDB data characterize only steady-state LTO emissions under standard atmospheric conditions, we used the extracted reference EIs as anchor points to fit emission characteristic curves. Furthermore, we introduced a dynamic environmental correction model by integrating second-level measured fuel flow and environmental parameters (temperature, pressure, humidity) provided by QAR. This process successfully transformed static standard emission data into dynamic EIs covering the full-flight phase (including LTO and CCD), achieving high-resolution quantification of instantaneous aircraft emissions under real-world meteorological conditions.

2.3 High-Precision Civil Aviation Emission Model

2.3.1Reference Emission Index Fitting

The QAR system records fuel flow rate at 1-Hz resolution independently for each engine, providing the engine-specific resolution required for the emission index fitting described below. Following the Mass Balance Principle, the generation of CO_2 and SO_2 primarily depends on the chemical composition of the fuel and is independent of engine operating conditions. In accordance with ICAO recommendations, we adopted fixed EIs of 3150 g/kg for CO_2 and 1 g/kg for SO_2 (Chen et al., 2021; Howitt et al., 2011).

For NO_x, HC, CO, and nvPM, which are significantly influenced by combustion efficiency, the ICAO EEDB provides discrete EI values only at four standard thrust settings (7%, 30%, 85%, and 100%), measured and certified on a per-engine basis under standardized test-bench conditions. These discrete values are not directly applicable to the continuous flight conditions

https://doi.org/10.5194/essd-2026-530
Preprint. Discussion started: 12 August 2026

recorded by QAR. Therefore, we constructed a continuous mapping function from single-engine fuel flow to reference EI (DuBois & Paynter, 2006), ensuring strict consistency between the EEDB calibration basis and the independent, engine-level fuel flow rate ($FF_{i,t}$) used as the input variable throughout this study.

We adopted different fitting strategies based on the formation mechanisms of different emissions. The generation rate of NO_x shows a strong positive correlation with combustor temperature (David, 2004; Lefebvre & Ballal, 2010); thus, a linear interpolation model was used. Conversely, HC, CO, and nvPM are mainly produced by incomplete combustion at low thrust and decay exponentially with increasing fuel flow; therefore, a power-law function was employed for fitting (Lee et al., 2010; Yim et al., 2013b). Through this method, we established corresponding reference emission index equations for every engine model in the dataset, expressed as a function of single-engine fuel flow:

$$EI_{x,ref} = f(FF_i) \tag{1}$$

Table 3 presents the fitted parameters for selected typical engines. The coefficient of determination (R^2) is calculated based on the linearized log-log transformation of the data, and generally higher than 0.95, verifying the high robustness of the fitted model in describing reference emission characteristics.

Table3: Fitting equations and results of mainstream engine models

Engine Type	HC			NO_x		
	$y=ax^b$			$y=ax+b$		
	a	*b*	R^2	*a*	*b*	R^2
CF6-80C2B5F	0.062	-1.933	0.997	8.668	4.537	0.970
CFM56-5A5	0.145	-1.009	0.986	22.836	2.254	0.998
CFM56-5B4/3	0.001	-3.195	0.999	15.830	3.078	0.992
CFM56-5B4/P	0.060	-1.916	0.997	22.556	2.374	0.998
CFM56-5B7/3	0.001	-3.195	0.979	15.830	3.078	0.992
CFM56-7B22E	0.001	-3.403	0.989	14.037	3.281	0.986
CFM56-7B24/3	0.001	-3.295	0.996	14.268	3.273	0.989
GP7270	0.021	-3.629	0.998	14.506	1.954	0.992
Trent 1000-A	0.010	-1.878	0.999	19.520	0.734	0.995
CF6-80A	0.253	-1.693	0.996	13.177	1.776	0.999
D-30 (II series)	0.043	-3.396	0.999	15.109	1.661	0.999
D-30KU-154	0.208	-2.611	0.997	9.553	1.009	0.999
Engine Type	**CO**			**PM**		

https://doi.org/10.5194/essd-2026-530
Preprint. Discussion started: 12 August 2026

	$y=ax^b$			$y=ax^b$		
	a	***b***	R^2	***a***	***b***	R^2
CF6-80C2B5F	0.902	-1.875	0.998	3.497	2.527	0.999
CFM56-5A5	0.357	-1.698	0.995	41.185	2.156	0.997
CFM56-5B4/3	0.306	-2.038	0.987	46.197	2.211	0.998
CFM56-5B4/P	0.243	-2.017	0.997	41.205	2.164	0.997
CFM56-5B7/3	0.306	-2.038	0.997	46.197	2.211	0.998
CFM56-7B22E	0.319	-2.066	0.999	41.804	2.156	0.996
CFM56-7B24/3	0.317	-2.066	0.986	41.315	2.186	0.997
GP7270	0.468	-2.942	0.998	41.125	2.174	0.998
Trent 1000-A	0.290	-2.354	0.991	241.552	1.998	0.989
CF6-80A	1.633	-1.503	0.999	1454.233	9.362	0.998
D-30 (II series)	3.193	-1.440	0.999	40.193	2.242	0.998
D-30KU-154	3.312	-2.003	0.999	40.394	2.131	0.997

2.3.2 Atmospheric Correction of Emission Indices

Since the reference EI obtained from Eq. (1) corresponds to sea-level, standard-day test-bench conditions, the single-engine reference EI must be further corrected for the actual ambient atmospheric state encountered during flight, using the BFFM2 framework (Baughcum et al., 1996). This model directly utilizes the Static Air Temperature (SAT) recorded by QAR as the ambient temperature (T_{amb}). Regarding ambient pressure (P_{amb}), considering that the Pressure Altitude (ALT_STDC) recorded by QAR characterizes the geopotential height under standard atmospheric pressure conditions, we converted it into actual ambient pressure by combining it with the standard barometric formula:

$$P_{amb} = P_b \times \left(1 - \frac{L \cdot (h - h_b)}{T_b}\right)^{\frac{g_0 \cdot M}{R \cdot L}} \tag{2}$$

where P_b and T_b are the reference baseline pressure and temperature, L is the temperature lapse rate of the troposphere, h is the pressure altitude recorded by QAR, h_b is the baseline height, g_0 is the gravitational acceleration, M is the molar mass of Earth's atmosphere, and R is the universal gas constant. Subsequently, with the standard thermodynamic Goff-Gratch equation, we utilized the calculated P_{amb} and measured T_{amb} to further deduce the instantaneous specific humidity and humidity correction factors (H). Finally, these second-level environmental parameters were input into the BFFM2 correction system to dynamically calibrate the Emission Indices of HC, CO, NO_x for each individual powerplant:

$$EI_{HC,i,t} = EI_{HC,ref} \times \frac{\theta_t^{3.3}}{\delta_t^{1.02}} \tag{3}$$

https://doi.org/10.5194/essd-2026-530
Preprint. Discussion started: 12 August 2026

$$EI_{CO,i,t} = EI_{CO,ref} \times \frac{\theta_t^{3.3}}{\delta_t^{1.02}} \tag{4}$$

$$EI_{NO_x,i,t} = EI_{NO_x,ref} \times \frac{\delta_t^{1.02}}{\theta_t^{3.3\times 0.5}} \times e^{H_t} \tag{5}$$

where δ_t and θ_t are the ambient pressure ratio and temperature ratio converted from QAR measured data at second t, respectively, and H_t is the humidity correction coefficient characterizing the inhibitory effect of ambient humidity on NO_x formation.

2.3.3 Emission Quantification

Building on the single-engine reference EI (Eq. 1) and its atmospheric correction (Eqs. 2-5), the total emission inventory is produced by independently evaluating and summing the contribution of each engine, rather than applying a bulk index to aggregated aircraft-level fuel flow. In real-world flight operations, particularly during ground taxiing and complex terminal maneuvers, aircraft frequently exhibit thrust asymmetry, such as the deliberate deployment of single-engine taxiing (SET) protocols for fuel conservation. To faithfully preserve these operational characteristics without introducing errors from non-linear averaging, this study conducts emission estimation strictly at the engine-specific level.

Specifically, the dynamic, atmospherically corrected emission index ($EI_{x,i,t}$) derived in Sect. 2.3.2 is mapped independently onto the instantaneous fuel flow rate of each engine. This engine-specific treatment is necessary because the reference EI-fuel flow relationships embedded in the EEDB are inherently non-linear (piecewise linear for NO_x, power-law for HC, CO, and nvPM); averaging the fuel flow of two engines prior to mapping would distort the resulting EI through Jensen's inequality, particularly under asymmetric thrust conditions such as SET. The instantaneous emission rate of pollutant species x for engine i at second t is therefore given by:

$$e_{x,i,t} = FF_{i,t} \times EI_{x,i,t}\left(FF_{i,t}, \delta_t, \theta_t, H_t\right) \tag{6}$$

where $FF_{i,t}$ is the measured fuel flow rate (kg/s) of engine i at time t, and δ_t, θ_t, H_t are the ambient pressure, temperature, and humidity correction factors defined in Eqs.(3-5). The total instantaneous emission rate of species x across the aircraft platform is obtained by synchronized summation over all active engines:

$$E_{x,t} = \sum_{i=1}^{N_{eng}} e_{x,i,t} \tag{7}$$

where N_{eng} denotes the number of active engines ($N_{eng} = 2$ for typical twin-engine aircraft, though this formulation naturally accommodates $N_{eng} = 1$ under SET conditions). The total emission mass of species x over the full flight duration T is obtained by summing Eq. (7) at the native 1-second QAR sampling resolution:

$$M_x = \sum_{t=1}^{T} E_{x,t} \times \Delta t \tag{8}$$

with $\Delta t = 1\,s$. This engine-disaggregated formulation ensures that the micro-level thermodynamic state of each engine is

https://doi.org/10.5194/essd-2026-530
Preprint. Discussion started: 12 August 2026

preserved throughout the inventory construction, providing a physically consistent and traceable basis for emission quantification under both symmetric and asymmetric thrust operations.

2.4 Inventory Uncertainty Evaluation

To systematically assess the accuracy and robustness of different aviation emission inventory approaches, we designed three parallel Monte Carlo experiments corresponding to estimation paths based on airborne measured parameters (QAR), surveillance data combined with performance models (ADS-B), and statistical flight data (SFD). Uncertainty sources across all three experiments were parameterized consistently to ensure comparability.

We modeled uncertainty differently depending on the physical nature of each quantity. For quantities with a natural zero point, such as fuel flow, pressure, flight distance, and operating time, we used a multiplicative relative error model, $N(1.0, \sigma^2)$, representing proportional fluctuations around the nominal value. For temperature, where measurement error is conventionally expressed in absolute rather than relative terms (Hersbach et al., 2020), we used an additive error model, $N(0, \sigma^2)$. Emission indices were modeled with a log-normal distribution, consistent with the log-normal spread typically observed in engine certification test data (Wasiuk et al., 2015). Fuel sulfur content was modeled with a truncated normal distribution to exclude non-physical negative values (Yim et al., 2015). Parameter settings for all quantities are summarized in Table 4.

Table 4: Configuration of uncertainty input parameters

Parameter	Error Type	PDF Form	QAR	ADS-B	SFD
Fuel flow	Multiplicative	$N(1.0, \sigma^2)$	σ=0.02	σ=0.15	σ=0.30
Ambient Pressure	Multiplicative	$N(1.0, \sigma^2)$	σ=0.02	σ=0.03	σ=0.05
Ambient Temperature	Additive	$N(0, \sigma^2)$	σ=0.5K	σ=1.0K	σ=5.0K
Taxi Time Factor	Multiplicative	$LogN(0, \sigma^2)$	-	-	σ=0.3
Trajectory Distance	Multiplicative	$N(\mu, \sigma^2)$	-	-	μ=0.93 σ=0.02
Emission Index(NO_x/others)	Multiplicative	$LogN(0, \sigma^2)$	σ=0.10 / 0.20		
Fuel Sulfur Content	Additive	Trunc $N(\mu, \sigma^2)$	μ=600ppm σ=150ppm		

Emission indices for all experiments were calculated using the ICAO EEDB (v31) and its associated correction models. To account for the difference between certification test-bench performance and in-service engine behavior, we applied a log-normal perturbation with a geometric standard deviation of 10% for NO_x and 20% for CO, HC, and PM (Wasiuk et al., 2015). Fuel sulfur content was modeled as a truncated normal distribution (mean 600 ppm, SD 150 ppm), based on global jet fuel sampling results (Kapadia et al., 2016). These parameters were held constant across all three data-source experiments to ensure

https://doi.org/10.5194/essd-2026-530
Preprint. Discussion started: 12 August 2026

comparability.

For the QAR experiment, uncertainty arises primarily from onboard sensor measurement accuracy. Error parameterization was anchored to standard avionics performance specifications (e.g., ARINC 706 for Air Data Systems) and typical engine manufacturer calibration tolerances. Fuel flow (FF) was modeled with a multiplicative error $N(1.0, 0.02^2)$ (±2% accuracy), ambient pressure (Pamb) with $N(1.0, 0.02^2)$, and SAT with an additive error $N(0, 0.5^2)$ (±0.5 °C accuracy) (ICAO, 2011).

For the ADS-B experiment, fuel flow is derived from a performance model rather than measured directly. Following EUROCONTROL BADA and the GAIA global aviation emissions database (Teoh et al., 2024), we set the multiplicative fuel flow error to $N(1.0, 0.15^2)$, reflecting structural model bias. Meteorological inputs were drawn from ERA5 reanalysis, with an additive temperature error of $N(0, 1.0^2)$ K and a multiplicative pressure error of $N(1.0, 0.03^2)$, consistent with the reported systematic bias of reanalysis products (Hersbach et al., 2020).

For the SFD experiment, environmental conditions default to the International Standard Atmosphere (ISA), which does not capture spatiotemporal variation in real meteorology; we set the corresponding temperature error to $N(0, 5.0^2)$ K, representing the typical bias between ISA and observed conditions (ICAO, 1993). To represent the systematic distance underestimation of great-circle routing relative to actual flight paths, we applied a multiplicative correction factor $N(0.93, 0.01^2)$, corresponding to an underestimation of approximately 7% - 8% (J. Wang et al., 2024). Taxi and holding times were modeled with a log-normal factor $LogN(0, 0.3^2)$, representing operational time variability of roughly ±30% (Simaiakis & Balakrishnan, 2016).

We performed Monte Carlo simulations for all three estimation frameworks, with N = 10,000 independent stochastic realizations per flight, each drawing input parameters from the distributions defined above. The nominal (unperturbed) emission estimate computed directly from measured QAR data is reported separately as the exact point estimate in Sect. 3.2; the Monte Carlo ensemble is used exclusively to characterize output uncertainty. We summarized the resulting output distribution using the coefficient of variation (CV) and further decomposed the sources of uncertainty using variance-based sensitivity analysis (VSA). Assuming error sources are statistically independent, their contributions to total emission variance can be approximated as a sum of first-order variance terms (Sobolʹ, 2001):

$$V_{total} \approx V_{FF} + V_{Env} + V_{Model} + V_{LTO} \tag{7}$$

where $V_{FF}, V_{Env}, V_{Model}$ and V_{LTO} represent the uncertainty contributions related to fuel flow, environmental parameters, emission indices, and operating time, respectively. The results of the uncertainty analysis and sensitivity attribution are discussed in detail in Sect. 3.2.

3 Results and Discussion

3.1 Overview of the 2023 China Aviation Emission Inventory

Leveraging high-frequency observations from approximately 4.52 million flights recorded by QAR, this study developed a four-dimensional emission inventory covering nationwide civil aviation activities in China throughout 2023. The inventory includes six major pollutants, namely CO_2, NO_x, SO_2, PM, CO, and HC. Inventory estimates indicate that the total fuel

https://doi.org/10.5194/essd-2026-530
Preprint. Discussion started: 12 August 2026

consumption of China's civil aviation sector reached 28.4 Mt in 2023. To evaluate the reliability of the inventory, the estimated fuel consumption was compared with the official statistics(CAAC, 2024) released by the CAAC. Based on the transport turnover and average fuel intensity reported by CAAC, the corresponding fuel consumption in 2023 was estimated to be approximately 25.03 Mt, whereas the inventory estimate obtained in this study was about 13.5% higher. This difference is primarily attributable to the distinct accounting frameworks adopted by the two approaches. The CAAC estimate is derived from aggregate transport turnover and average fuel intensity, and therefore mainly reflects the average operational efficiency of the air transport system. In contrast, the present inventory is largely from direct observations of fuel flow during actual flight operations, allowing fuel consumption associated with taxiing, air traffic flow management, holding patterns, and weather-related rerouting to be explicitly represented. More fundamentally, transport turnover is a measure of transportation output rather than actual flight activity, and therefore may not fully capture fuel consumption arising from operational inefficiencies and non-productive flight processes. Furthermore, the QAR data used in this study covers approximately 4.52 million flights, accounting for 96.8% of all commercial flight movements reported by CAAC in 2023. Such extensive coverage suggests that the inventory provides a highly representative characterization of actual civil aviation operations in China. Therefore, the observed difference is more likely attributable to discrepancies in accounting methodologies and statistical definitions rather than systematic biases resulting from incomplete flight coverage. Figure S3 further illustrates the monthly variations in flight volume and total emissions for the six pollutants in the 2023 inventory.

To assess the consistency of the present inventory with previous studies and to investigate the sources of discrepancies among different estimation approaches, Table 4 compares the inventory with several recent aviation emission inventories developed using SFD, ADS-B trajectories, and other activity datasets. Overall, the estimates show broad agreement in terms of fuel consumption and major pollutant emissions, although notable differences remain for specific species. Considering the formation mechanisms of individual pollutants and their sensitivity to flight operating conditions, these differences can be broadly categorized into three groups: (1) fuel consumption, CO_2, and SO_2, which are primarily determined by fuel burn; (2) CO and HC, which are associated with incomplete combustion processes; and (3) NO_x and PM, which are highly sensitive to engine thermodynamic conditions.

Fuel consumption, CO_2, and SO_2 emissions are generally consistent with previous studies. The inventory estimates total fuel consumption, CO_2 emissions, and SO_2 emissions of 28.4 Mt, 89.3 Mt, and 28.4 kt, respectively, for China's civil aviation sector in 2023. Compared with recent aviation emission inventories developed using ADS-B trajectories or other activity datasets, the estimates fall within a comparable range, indicating broad agreement in the characterization of overall aviation energy consumption. Since both CO_2 and SO_2 emissions are directly linked to fuel burn, the three variables exhibit similar patterns. Differences among studies are primarily associated with variations in study year, flight activity levels, spatial coverage, and fuel-consumption estimation approaches, while the overall magnitude remains generally consistent.

CO and HC emissions are mainly governed by incomplete combustion processes. As typical products of incomplete fuel oxidation, the formation of CO and HC is sensitive to low-thrust operating conditions and combustion efficiency. The inventory estimates CO and HC emissions of 44.3 kt and 6.35 kt, respectively. CO emissions are at the lower end of the range reported in previous studies and are even lower than some estimates focusing solely on the LTO cycle, whereas HC emissions are broadly consistent with existing inventories. These differences are largely attributable to variations in the treatment of taxiing, idling, and other low-thrust operating conditions. Because CO formation is highly sensitive to incomplete combustion, its emissions respond more strongly to changes in engine operating conditions. In contrast, HC emissions are generally lower in magnitude and exhibit a relatively weaker response to operational variability, leading to better agreement among different studies.

NO_x and PM emissions are highly sensitive to engine thermodynamic conditions. The inventory estimates NO_x and PM emissions of 634.6 kt and 8.46 kt, respectively, placing them toward the upper range of values reported in the literature. Unlike CO and HC, the formation of NO_x and particulate matter is primarily controlled by combustion temperature, combustor pressure, and engine load. As a result, these pollutants are more sensitive to variations in flight phase and atmospheric conditions. In particular, high-thrust operations during takeoff and climb substantially increase combustor temperatures, promoting NO_x formation and particulate matter emissions. Differences among inventories in engine-performance assumptions, environmental correction schemes, and representations of operating conditions can therefore lead to substantial variations in estimated NO_x and PM emissions. Consequently, compared with fuel consumption and CO_2 emissions, NO_x and PM generally exhibit greater variability across different aviation emission inventories.

Table 5: Comparison of total annual emissions from China's civil aviation across different inventories

Inventory	Source	Year	CO/kt	HC/kt	PM/kt	SO_2/kt	NO_x/kt	CO_2/Mt
Our study	QAR	2023	44.3	6.35	8.46	28.4	634.6	89.3
Ma et al. (2024)	AIP	2019	58.2	5.03	3.2	36.2	349.9	86.7
Zhang et al.(2022)	ADS-B	2018	-	14.3	1.64	21.3	477.2	81.3
Lang et al. (2024)	ADS-B	2023(LTO)	46.1	3.2	1.1	18.4	62.3	-
Fan et al. (2012)	Great-circle	2010	39.7	4.6	-	9.7	154.1	38.21
Liu et al. (2019)	Great-circle	2015	59.6	4.77	3.32	19	304.8	59.96

3.2 Sources of Systematic Bias and Uncertainty Propagation Mechanisms

As shown in Figure 2, the Monte Carlo simulation results demonstrate a clear tiered difference in estimation precision across the three parallel experiments. SFD estimates are the least accurate, dominated by systematic underestimation of flight distance relative to actual trajectories, which propagates into systematically low emission totals. Both ADS-B and QAR methods use observed trajectories and therefore largely avoid this geometric bias; the QAR method further benefits from second-level sampling and measured onboard parameters, yielding lower variance across all pollutant categories examined below.

For fuel-flow controlled species (CO_2, SO_2), the value of measured data lies in replacing generic model assumptions with direct observation. The ADS-B method corrects trajectory geometry but still derives fuel flow semi-empirically from the BADA performance model, leaving a CO_2 estimation CV of 14.9%. The QAR-based method, using measured fuel flow directly, reduces this to 2.0%, which is consistent with the expected precision of onboard fuel flow sensors (Olsen et al., 2013). The SFD method, relying entirely on standard taxi-time and distance assumptions, shows the largest error (CV = 30.0%), compounding trajectory underestimation with a constant taxiing-time assumption.

For NO_x, which is sensitive to combustor thermodynamic conditions, the resolution of environmental input data becomes the limiting factor. The ADS-B method, typically corrected using ERA5 reanalysis meteorology, improves on the SFD model's static ISA assumption, but the coarser spatiotemporal resolution of reanalysis data still cannot capture transient combustor-inlet conditions during rapid thrust changes. The QAR method, which couples second-level Total Air Temperature and total pressure measurements directly from onboard sensors, captures the transients, including extreme combustor conditions during high-thrust climb or high ambient-temperature operations, reducing NO_x estimation uncertainty to CV = 10.6%, compared with 28.9% (ADS-B) and 52.7% (SFD).

For incomplete-combustion products (HC, CO), the advantage of high-resolution data is largest, because these pollutants are generated primarily during ground taxiing and idle operation, where the emission index rises steeply and non-linearly. Small errors in estimated idle duration are therefore amplified disproportionately in the resulting HC/CO estimate. The SFD model, which lacks real ground-operation data, shows the largest error of any pollutant-method combination (HC CV = 177.4%). ADS-B data, constrained by intermittent ground coverage and lower sampling rates, cannot reliably resolve the frequent start-stop idle behavior typical of taxiing. QAR's continuous 1 Hz recording across the full flight envelope directly captures the duration of low-thrust conditions, avoiding this error amplification.

Taken together, these results indicate that trajectory correction alone, as achieved by ADS-B, is sufficient to address geometric distance bias, but not the errors arising from performance-model-derived fuel flow and environmental conditions. Only direct physical measurement, as provided by QAR, constrains both the activity baseline and the thermodynamic inputs needed for emission index calculation, which is why its precision advantage grows from CO_2/SO_2 to NO_x to HC/CO, precisely the pollutants most sensitive to non-linear, thrust-dependent formation processes.

https://doi.org/10.5194/essd-2026-530
Preprint. Discussion started: 12 August 2026

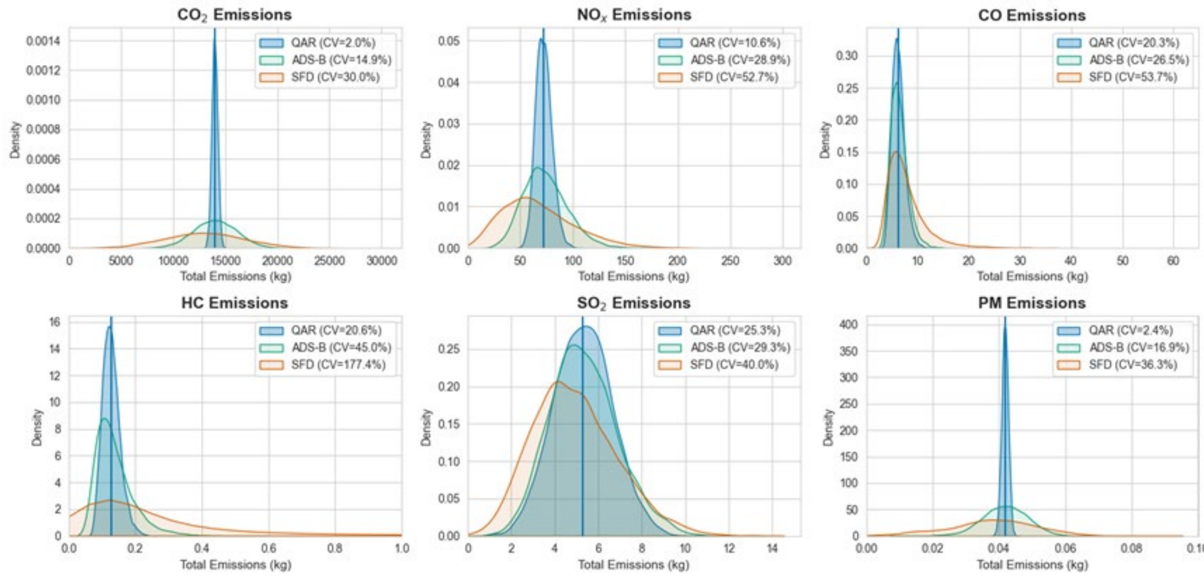

Figure 2: Probability density functions of estimated emissions for six pollutants across different inventory compilation methods.

Because the formation of incomplete-combustion products (CO, HC) is highly sensitive to low-thrust conditions and combustion efficiency, as shown in Figure 3, we applied VSA to these pollutants to characterize how the dominant sources of estimation error shift across data sources.

For the SFD method, which uses no measured data, error is dominated by operational assumptions: fixed LTO segment durations account for 55.2% of total variance and generic fuel-flow model bias for 31.0%, together explaining most of the estimation error. This is consistent with prior findings that fixed-duration procedures and averaged performance parameters are a primary source of distortion in traditional LTO based inventories (Akçelik & Besley, 2003).

Moving to the ADS-B method, real trajectories largely resolve the duration-related error, but the center of gravity of the error shifts rather than shrinks: constrained by its reliance on a semi-empirical fuel model and static environmental inputs, the EI model itself now accounts for 73.5% of total variance, overtaking fuel-model bias (26.5%). In other words, once activity-level timing is corrected, the model's inability to represent combustion efficiency under varying operating conditions becomes the binding constraint on precision.

With the QAR method, direct coupling of real trajectories, second-level fuel flow, and onboard thermodynamic measurements removes most of the error associated with activity and environmental inputs: instrument measurement uncertainty contributes only 2.0% of total variance, while the remaining 98.0% is attributable to the fitting residual of the EEDB emission model itself. This shift indicates that, once activity and environmental inputs are constrained by direct observation, inventory precision is no longer limited by data resolution but by the residual gap between EEDB reference curves and real-world engine behavior across the full range of in-service operating conditions.

https://doi.org/10.5194/essd-2026-530
Preprint. Discussion started: 12 August 2026

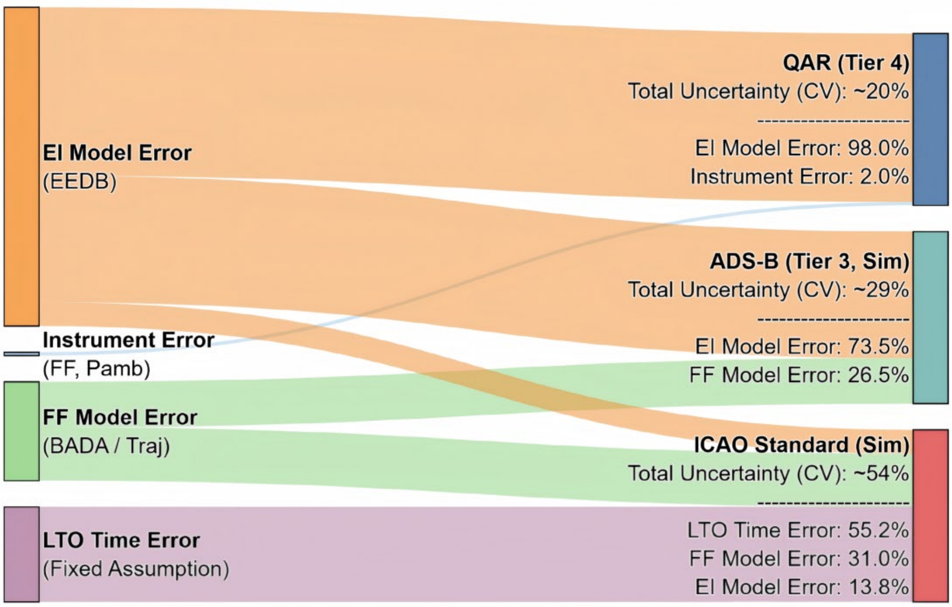

Figure 3: Variance-based sensitivity analysis of error source attribution for CO/HC emissions across different inventory compilation methods， width of the flows represents the proportion of variance contribution

3.3 Temporal Evolution Characteristics

Figure 4 shows the relative contribution of each flight phase to total emissions in the 2023 QAR dataset. The Cruise phase dominates cumulative emissions for most pollutants, reflecting its share of total flight duration: it accounts for 47.8% of total fuel consumption (and, correspondingly, CO_2 and SO_2, whose emission indices scale linearly with fuel burn regardless of thrust setting), 39.6% of HC, 39.1% of CO, 35.5% of NO_x, and 27.6% of PM.

This duration-driven dominance does not hold for pollutants governed by combustion efficiency rather than fuel throughput. HC and CO formation increases as combustion efficiency falls (Liu et al. 2019), so both are concentrated during low-power ground operations: taxiing contributes 23.7% of total HC (16.3% Taxi Out, 7.4% Taxi In) and 19.4% of total CO (12.7% Taxi Out, 6.7% Taxi In), consistent with the longer duration of taxi-out queuing relative to taxi-in. Under idle thrust, lower combustor temperature and pressure impair fuel atomization and mixing, sharply raising HC and CO generation rates (Lee et al., 2010; Ma et al., 2025).

PM follows the opposite pattern, peaking not under low-thrust but high-thrust conditions: the 2-Segment Acceleration phase alone contributes 18.0% of total PM despite its short duration, consistent with the soot formation mechanism described by Lobo (2020), in which high-temperature, high-pressure combustion during climb drives a non-linear increase in soot nucleation and growth. Taken together, these phase-resolved contributions show that no single phase dominates across all pollutants: fuel-scaling species (CO_2, SO_2) track flight duration, while HC/CO and PM peak under opposite thrust regimes, reflecting their

https://doi.org/10.5194/essd-2026-530
Preprint. Discussion started: 12 August 2026

distinct formation mechanisms. This distinction is only resolvable through phase-level QAR segmentation, and has direct implications for where near-airport air quality impacts are concentrated.

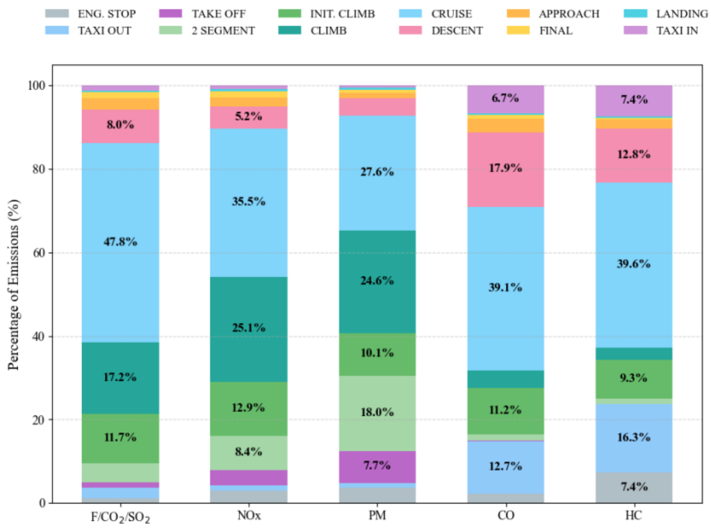

Figure 4: Distribution proportions of fuel consumption and pollutant emissions across twelve refined flight phases.

To examine the microscopic response of pollutant formation to flight conditions, we selected a representative B737-800 flight to construct a full-flight, temporal resolution in second emission profile (Figure 5). The profile reveals distinct, thrust-dependent non-linearities across pollutant species that are not resolvable at coarser temporal resolution.

During takeoff and climb, two separate mechanisms operate concurrently under high thrust. CO_2 and SO_2 track fuel flow directly, peaking instantaneously with the surge in fuel consumption, since both are stoichiometric combustion products scaling with fuel burn rather than combustor temperature. In parallel, the high-temperature, high-pressure combustor environment promotes rapid formation of thermal NO_x and non-volatile PM through temperature-dependent reaction pathways, producing peaks that align with, but are mechanistically distinct from, the fuel-flow-driven CO_2/SO_2 peaks. The climb-phase profile also shows sawtooth-shaped fluctuations in several species, consistent with the frequent thrust adjustments pilots make in response to air traffic control instructions and turbulence. This transient structure is smoothed out entirely by inventory methods that assume emissions decay monotonically with altitude, and is only visible at second-level resolution.

During steady-state cruise, combustion efficiency is near-optimal: CO_2 and NO_x emission rates stabilize, while CO and HC concentrations fall to near-zero baseline levels, indicating near-complete fuel oxidation under sustained high-temperature, high-pressure conditions. The pattern reverses during descent and approach. As thrust drops to idle or low-power settings, combustor temperature falls and reaction rates slow correspondingly; CO and HC concentrations rebound sharply and fluctuate with frequent throttle adjustments during the approach sequence. A further, distinct CO/HC spike occurs during taxi, consistent with sustained low-power ground operation, while thrust reverser deployment at landing produces a separate transient spike likely associated with combustion instability during the rapid thrust transition rather than low-power operation per se(Schürmann et al., 2007). Together, these results indicate that inventories relying on averaged or phase-mean emission factors systematically underestimate short-duration pollution peaks near airports, precisely the events most relevant to near-ground air quality exposure (Woody et al., 2011).

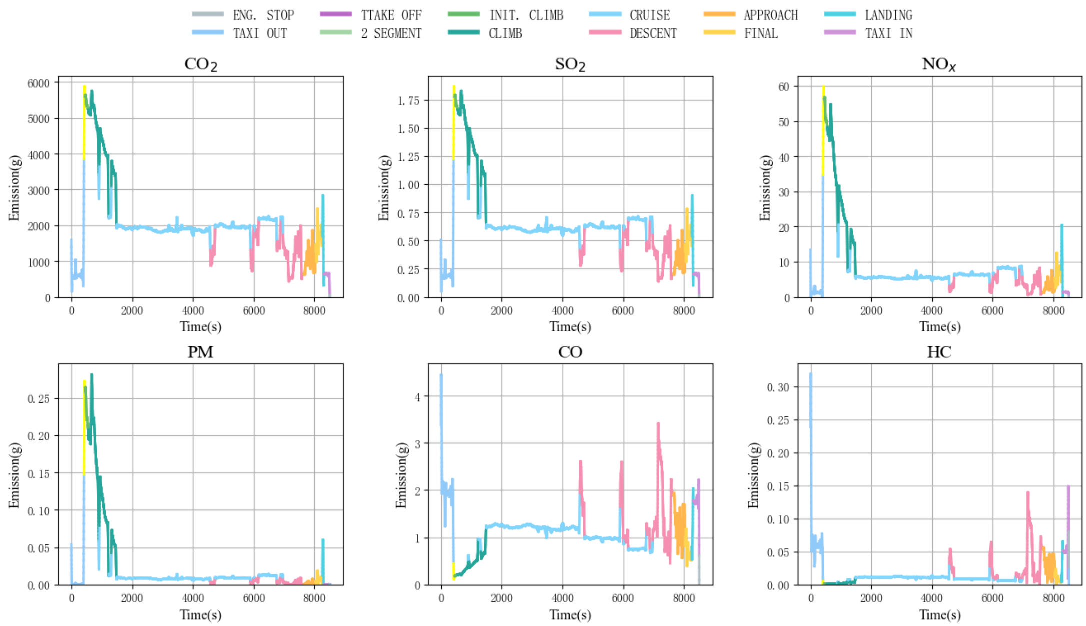

Figure 5: High-frequency emission profiles of a typical flight.

3.4 Spatial Dimension Analysis

3.4.1 Reconstruction of 3D Flight Trajectories and Emission Characteristics for Typical Routes

Using high-frequency QAR data with 0.001° longitude/latitude precision, ~0.03 m (0.1 ft) altitude precision, and 1 s temporal resolution, we reconstructed three-dimensional flight trajectories and vertical profiles for all flights between Beijing Capital International Airport (ZBAA) and Chengdu Tianfu International Airport (ZUTF) in March 2023. This route was selected as a representative case for detailed trajectory-level analysis: it is one of the trunk corridors identified in the network-level analysis above, its ~1,600 km stage length is long enough to capture a full climb–cruise–descent profile without truncation by short-haul operating constraints, and both endpoints are high-frequency hub airports, providing a large and consistent sample within a single month.

Figure 6(a) shows that the observed three-dimensional tracks depart substantially from the ideal great-circle route, forming multi-segment polylines. Divergence and distortion are concentrated in the terminal areas around both airports, where trajectory bundles spread across a wider range of headings during low-altitude approach and departure, which is consistent with sequencing and holding operations under air traffic control guidance (del Pozo Domínguez et al., 2023). Figure 6(b) shows a corresponding fine structure in the vertical dimension: outbound and inbound cruise altitudes are strictly stratified, consistent with the odd/even altitude allocation under RVSM rules (ICAO, 2001).

https://doi.org/10.5194/essd-2026-530
Preprint. Discussion started: 12 August 2026

Figure 6(c) shows how this trajectory structure translates into the vertical distribution of CO_2 emissions. Above 3,000 m, the cruise (CCD) phase accounts for approximately 80.8% of total emissions on this route, with a cumulative peak near 9,600 m corresponding to the altitude at which aircraft hold steady cruise conditions to minimize fuel burn. Below 3,000 m, by contrast, flight distance accounts for only 10.1% of the route total but contributes 19.2% of CO_2 emissions, a result of the high-thrust climb, frequent thrust adjustments, and taxiing associated with the LTO cycle, which raise emission intensity per unit distance well above cruise-phase levels. Because this low-altitude emission is concentrated close to the surface and near populated terminal areas, it is of particular relevance to local air quality assessment(Y. Wang et al., 2023).

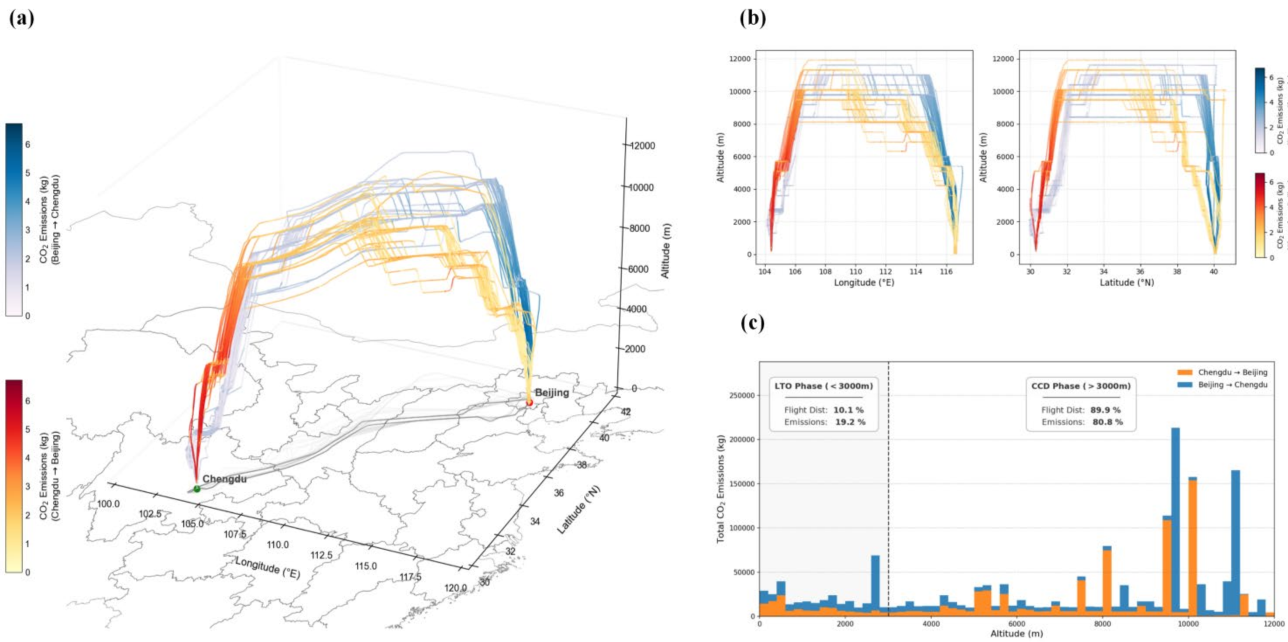

Figure 6: (a) Three-dimensional visualization of real-world flight trajectories between Beijing (ZBAA) and Chengdu (ZUTF), colored by instantaneous CO_2 emission rates. (b) Orthogonal projections of flight trajectories for the ZBAA–ZUTF route onto longitude-altitude and latitude-altitude planes, where blue and orange-red spectra denote outbound (to Chengdu) and inbound (to Beijing) flights, respectively. (c) Vertical profile of total accumulated CO_2 emissions for the ZBAA–ZUTF route, aggregated in 200 m altitude bins.

3.4.2 Analysis of High-Resolution Spatial Pattern of Aviation Carbon Emissions in China

Figure 7(a) shows that the spatial distribution of aviation carbon emissions closely tracks China's economic geography, with a pronounced east-west gradient. The Beijing-Tianjin-Hebei, Yangtze River Delta, and Pearl River Delta agglomerations are linked by a dense route network that produces continuous high-flux coverage across the eastern coastal and central regions. The western region, by contrast, shows a sparser, radial pattern centered on regional hubs such as Urumqi and Kunming, consistent with the concentration of air transport demand in areas of higher economic activity and population density.

https://doi.org/10.5194/essd-2026-530
Preprint. Discussion started: 12 August 2026

At finer spatial resolution, this pattern resolves into a hub-and-corridor structure. Continuous high-value pixels trace national trunk routes such as Beijing-Shanghai, Beijing-Guangzhou, and Shanghai-Chengdu, corresponding to the steady fuel consumption of the cruise (CCD) phase at high altitude. The localized emission hotspots at route endpoints instead reflect the accumulation of high-thrust, high-frequency LTO operations in near-ground airspace. Cruise emissions therefore appear as continuous linear flux along corridors, while LTO emissions appear as point-like concentrations at airports.

Figure 7(b) quantifies this east-west inequality: the meridional cumulative curve rises sharply east of 100°E, and the zonal curve peaks near 30°N, consistent with the role of the Yangtze River Economic Belt as the primary corridor linking eastern, central, and western air traffic. Figure 7(c) shows that emissions are highly concentrated at the grid level, with the top 10% of grid cells accounting for 74.2% of total CO_2 emissions. This concentration indicates that a small number of trunk corridors and hub airports account for a disproportionate share of aviation's carbon footprint, which is relevant to where operational or routing interventions would have the greatest effect on total emissions.

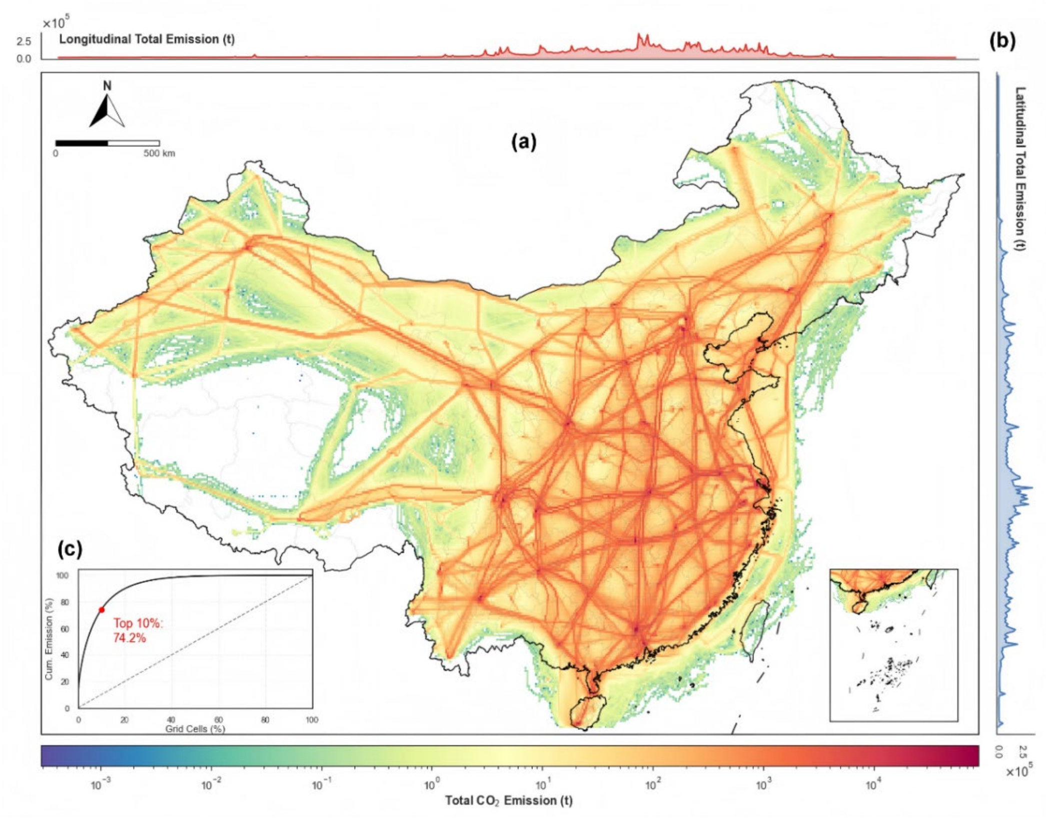

Figure 7: (a) Spatial intensity map illustrating the geographical distribution of emission loads. (b) Latitudinal and longitudinal marginal cumulative profiles, depicting the directional accumulation of emissions. (c) The Lorenz curve quantifies the spatial inequality and concentration of emissions.

To assess whether the hub-and-corridor pattern identified above is statistically significant, we conducted a spatial autocorrelation analysis on 0.1° × 0.1° gridded emissions. Figure 8(a) shows pronounced spatial clustering: High-High units

https://doi.org/10.5194/essd-2026-530
Preprint. Discussion started: 12 August 2026

Open Access Earth System Science Data Discussions

align closely with trunk routes such as Beijing–Shanghai, Beijing-Guangzhou, and Shanghai-Chengdu, connecting the hub cities of Beijing, Shanghai, Guangzhou, and Chengdu, while Low-Low units cover most of the non-route areas in the northwest and interior. Emissions are therefore not spatially diffuse but organized along the route network itself.

This clustering is confirmed by the global Moran's I (0.3389, $p < 0.05$) and by the quadrant distribution in Figure 8(b), where samples concentrate almost entirely in the High-High and Low-Low quadrants, with very few falling in the High-Low or Low-High transition quadrants. The scarcity of transition cases is consistent with the physical constraint that air traffic is confined to narrow, fixed-width corridors: emissions drop sharply outside a route's footprint rather than tapering gradually, leaving little room for intermediate grid values.

Figure 8(c) shows that grid-level emissions follow a power-law distribution, with a small number of high-load grid cells accounting for a disproportionate share of the cumulative total. Combined with the LISA results, this indicates that China's aviation emissions are concentrated both structurally, along a limited set of corridors and hubs and statistically, in a small subset of grid cells that dominate the national total.

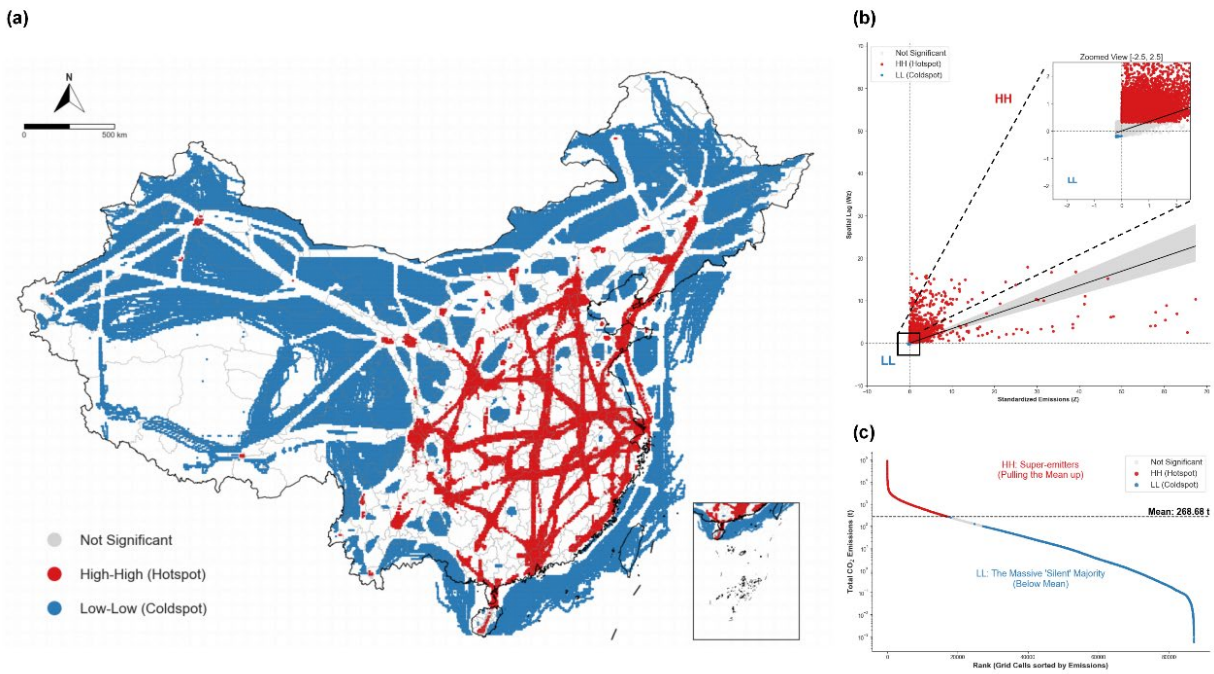

Figure 8: (a) LISA (Local Indicators of Spatial Association) cluster map showing local spatial agglomeration types. (b) Moran's scatter plot illustrating global spatial auto correlation. (c) Rank-size distribution plot revealing the heavy-tailed characteristic of emission intensity across grid cells.

4 Data availability

The high-resolution 4D gridded aviation emission inventory dataset generated in this study is freely available at Zenodo via

https://doi.org/10.5194/essd-2026-530
Preprint. Discussion started: 12 August 2026

https://doi.org/10.5281/zenodo.20828076 (Lu et al., 2026). The dataset is provided in GeoTIFF format with a spatial resolution of $0.1° \times 0.1°$, including emission fields for CO_2, NO_x, SO_2, PM, CO, and HC.

5 Conclusion

This study developed a four-dimensional aviation emission inventory for China's civil aviation sector in 2023, built directly from onboard measurements recorded by the Quick Access Recorder (QAR) system across more than 4.52 million flights, approximately 96.8% of commercial flight movements reported by the Civil Aviation Administration of China (CAAC). By coupling second-level fuel flow with observed trajectories and onboard environmental measurements, the inventory represents aviation emissions as they occur under real operating conditions, rather than as reconstructed from schedule- or trajectory-only proxies.

For 2023, the inventory estimates total fuel consumption of 28.4 Mt, corresponding to 89.3 Mt CO_2, 634.6 kt NO_x, 44.3 kt CO, 6.35 kt HC, 28.4 kt SO_2, and 8.46 kt PM. Fuel consumption, CO_2, and SO_2 estimates are consistent with the range reported in recent inventories, while larger discrepancies remain for CO, HC, NO_x, and PM, pollutants whose formation is governed by non-linear, thrust-dependent combustion processes rather than fuel throughput alone, and which existing inventories typically approximate using averaged emission factors.

This distinction is borne out directly by the uncertainty analysis: relative to ADS-B/BADA or schedule-based approaches, the QAR-based inventory reduces the coefficient of variation for CO_2 and PM to approximately 2%, reflecting the near-complete removal of activity-level and fuel-model uncertainty once real trajectories and measured fuel flow are used. For the combustion-sensitive species, the QAR framework similarly compresses the CV to 10.6% for NO_x, 20.3% for CO, and 20.6% for HC, markedly outperforming the ADS-B (26.5% - 45.0%) and SFD (52.7% - 177.4%) estimates. The residual uncertainty that remains is concentrated in the fitting of the EEDB emission model itself rather than in activity or environmental inputs indicating that further precision gains now depend on improving emission factor parameterization rather than on higher-resolution activity data.

The value of second-level observation is most apparent in the phase- and second-resolved results. Cruise operations, consistent with their share of flight duration, dominate fuel consumption and CO_2/NO_x emissions (47.8% and 35.5%, respectively), while HC is disproportionately concentrated in taxiing (23.7%) and PM in the short high-thrust acceleration segment preceding climb (18.0%). These patterns are consistent with distinct, thrust-dependent formation mechanisms, fuel-scaling for CO_2/SO_2, combustion-efficiency-limited for HC/CO, and temperature/pressure-driven soot nucleation for PM, and are only resolvable at the temporal resolution QAR data provide.

These process-level differences aggregate into pronounced spatial structure at the national scale. Emissions are vertically stratified by cruise-altitude allocation and horizontally concentrated, with the top 10% of grid cells accounting for 74.2% of national CO_2 emissions and significant clustering (Global Moran's I = 0.3389, $p < 0.05$) around the Beijing-Tianjin-Hebei, Yangtze River Delta, Pearl River Delta, and Chengdu-Chongqing regions. This concentration reflects the compounding of two effects identified above: aviation activity itself is concentrated along major economic corridors, and within that activity, LTO-phase emissions are further concentrated near a small number of high-frequency hub airports.

Taken together, these results show that direct physical observation improves aviation emission inventories not only by reducing aggregate uncertainty, but by resolving processes, transient thrust changes, idle-phase combustion inefficiency, near-airport LTO concentration, that averaged or trajectory-only methods cannot represent at all. The inventory provides second-level temporal resolution and nationwide coverage, offering a basis for near-airport air quality assessment and for evaluating the assumptions underlying existing lower-resolution aviation emission inventories.

Author contributions

LB and SL: Conceptualization, visualization and writing (original draft preparation). WC and WX: Data curation, Funding acquisition and Project administration. SH: Writing (review and editing). GQ and WX: Investigation and Validation.

Competing interests

The author has declared that they and their co-authors have no competing interests.

Financial support

Research presented in this paper was funded by National Natural Science Foundation of China (NSFC: 42571480) and an open grant from Key Laboratory of Green Airport, CAAC.

References

Abrahamson, J. P., Zelina, J., Andac, M. G., and Vander Wal, R. L.: Predictive model development for aviation black carbon mass emissions from alternative and conventional fuels at ground and cruise, Environ. Sci. Technol., 50, 12048–12055, https://doi.org/10.1021/acs.est.6b03749, 2016.

Akçelik, R. and Besley, M.: Operating cost, fuel consumption, and emission models in aaSIDRA and aaMOTION, in: 25th Conference of Australian Institutes of Transport Research (CAITR 2003), Adelaide, South Australia, 2003.

Barrett, S. R. H., Britter, R. E., and Waitz, I. A.: Global mortality attributable to aircraft cruise emissions, Environ. Sci. Technol., 44, 7736–7742, https://doi.org/10.1021/es101325r, 2010.

Baughcum, S. L., Tritz, T. G., Henderson, S. C., and Pickett, D. C.: Scheduled Civil Aircraft Emission Inventories for 1992: Database Development and Analysis, NASA Contractor Report 4700, NASA Langley Research Center, Hampton, VA, 1996.

CAAC: 2023 Civil Aviation Industry Development Statistical Bulletin, Civil Aviation Administration of China, available at: https://www.caac.gov.cn/XXGK/XXGK/TJSJ/202405/t20240531_224333.html (last access: 30 December 2025), 2024.

Chen, B., Yakovlev, A. A., and Moshkov, P. A.: Fast prediction method of aircraft noise with distributed propulsion in the far field, J. Phys. Conf. Ser., 1925, 012007, https://doi.org/10.1088/1742-6596/1925/1/012007, 2021.

Cui, Q., Chen, B., and Lei, Y.: Accounting for the aircraft emissions of China's domestic routes during 2014–2019, Sci. Data, 9, 383, https://doi.org/10.1038/s41597-022-01494-0, 2022.

Dannet, G., Bellouin, N., and Boucher, O.: Airspace restrictions due to conflicts increased global aviation's carbon dioxide emissions in 2023, Commun. Earth Environ., 6, 52, https://doi.org/10.1038/s43247-024-01956-w, 2025.

David, L. D.: Water Misting and Injection of Commercial Aircraft Engines to Reduce Airport NO_x, NASA Contractor Report, NASA/CR-2004-213032, https://doi.org/10.1021/es101325r, 2004.

del Pozo Domínguez, M., Leonés, J. L., Morales, M. P., and Astorga, R. V.: Assessing the environmental impact of Continuous Descent Operations based on Quick Access Recorder and surveillance data, in: 2023 IEEE/AIAA 42nd Digital Avionics Systems Conference (DASC), Barcelona, Spain, 1–9, https://doi.org/10.1109/DASC58513.2023.10311191, 2023.

Dong, J., Wang, C., and Sun, H.: Estimation of China's civil aviation flight emission inventory based on QAR, Acta Sci. Circumst., 42, 1–11, https://doi.org/10.13671/j.hjkxxb.2022.0224, 2022.

DuBois, D. and Paynter, G. C.: "Fuel Flow Method 2" for estimating aircraft emissions, SAE Trans., 115, 1–14, https://doi.org/10.4271/2006-01-1987, 2006.

EASA: ICAO Aircraft Engine Emissions Databank, European Union Aviation Safety Agency, available at: https://www.easa.europa.eu/en/domains/environment/icao-aircraft-engine-emissions-databank (last access: 30 December 2025), 2025.

European Environment Agency: EMEP/EEA air pollutant emission inventory guidebook 2023: Technical guidance to prepare national emission inventories, Publications Office of the European Union, Luxembourg, https://doi.org/10.2800/795737, 2023.

Fan, W., Sun, Y., Zhu, T., and Wen, Y.: Emissions of HC, CO, NO_x, CO2, and SO2 from civil aviation in China in 2010, Atmos. Environ., 56, 52–57, https://doi.org/10.1016/j.atmosenv.2012.03.052, 2012.

Gariel, M., Srivastava, A. N., and Feron, E.: Trajectory clustering and an application to airspace monitoring, IEEE Trans. Intell. Transp. Syst., 12, 1511–1524, https://doi.org/10.1109/TITS.2011.2160628, 2011.

Graver, B., Zhang, K., and Rutherford, D.: CO2 emissions from commercial aviation 2018, International Council on Clean Transportation (ICCT), Washington, DC, 2019.

Grewe, V., Gangoli Rao, A., Grönstedt, T., Xisto, C., Linke, F., Melkert, J., Middel, J., Ohlenforst, B., Blakey, S., Christie, S., Matthes, S., and Dahlmann, K.: Evaluating the climate impact of aviation emission scenarios towards the Paris agreement including COVID-19 effects, Nat. Commun., 12, 3841, https://doi.org/10.1038/s41467-021-24091-y, 2021.

https://doi.org/10.5194/essd-2026-530
Preprint. Discussion started: 12 August 2026

Hersbach, H., Bell, B., Berrisford, P., Hirahara, S., Horányi, A., Muñoz-Sabater, J., Nicolas, J., Peubey, C., Radu, R., Schepers, D., Simmons, A., Soci, C., Abdalla, S., Abellan, X., Balsamo, G., Bechtold, P., Biavati, G., Bidlot, J., Bonavita, M., et al.: The ERA5 global reanalysis, Q. J. Roy. Meteor. Soc., 146, 1999–2049, https://doi.org/10.1002/qj.3803, 2020.

Howitt, O. J. A., Carruthers, M. A., Smith, I. J., and Rodger, C. J.: Carbon dioxide emissions from international air freight, Atmos. Environ., 45, 7036–7045, https://doi.org/10.1016/j.atmosenv.2011.09.051, 2011.

IATA: IATA Annual Review 2024, International Air Transport Association, Geneva, Switzerland, 2024.

ICAO: Manual of the ICAO Standard Atmosphere (extended to 80 kilometres (262 500 feet)), Doc 7488-CD, International Civil Aviation Organization, Montreal, Canada, 1993.

ICAO: Guidance Material on the Implementation of a 300 m (1 000 ft) Vertical Separation Minimum (VSM) in the EUR Region, EUR Doc 009, International Civil Aviation Organization, Paris, France, 2001.

ICAO: Airport Air Quality Manual, Doc 9889, International Civil Aviation Organization, Montreal, Canada, 2011.

ICAO: ICAO Carbon Emissions Calculator, International Civil Aviation Organization, available at: https://www.icao.int/environmental-protection/environmental-tools/icec (last access: 30 December 2025), 2017.

Johansson, D. J. A., Azar, C., Pettersson, S., Sterner, T., Stettler, M. E. J., and Teoh, R.: The social costs of aviation CO2 and contrail cirrus, Nat. Commun., 16, 8558, https://doi.org/10.1038/s41467-025-64355-5, 2025.

Kapadia, Z. Z., Spracklen, D. V., Arnold, S. R., Borman, D. J., Mann, G. W., Pringle, K. J., Monks, S. A., Reddington, C. L., Benduhn, F., Rap, A., Scott, C. E., Butt, E. W., and Yoshioka, M.: Impacts of aviation fuel sulfur content on climate and human health, Atmos. Chem. Phys., 16, 10521–10541, https://doi.org/10.5194/acp-16-10521-2016, 2016.

Kim, B. Y., Fleming, G. G., Lee, J. J., Waitz, I. A., Clarke, J.-P., Balasubramanian, S., Malwitz, A., Klima, K., Locke, M., Holsclaw, C. A., Maurice, L. Q., and Gupta, M. L.: System for assessing Aviation's Global Emissions (SAGE), Part 1: Model description and inventory results, Transport. Res. D-Tr. E., 12, 325–346, https://doi.org/10.1016/j.trd.2007.03.007, 2007.

Koudis, G. S., Hu, S. J., North, R. J., Majumdar, A., and Stettler, M. E. J.: The impact of aircraft takeoff thrust setting on NO_x emissions, J. Air Transp. Manag., 65, 191–197, https://doi.org/10.1016/j.jairtraman.2017.06.009, 2017.

Lang, J., Yang, Z., Zhou, Y., Wen, C., and Cheng, X.: Four-dimensional aircraft emission inventory dataset of Landing and takeoff cycle in China (2019–2023), Earth Syst. Sci. Data, https://doi.org/10.5194/essd-2024-494, 2024.

Lee, D. S., Pitari, G., Grewe, V., Gierens, K., Penner, J. E., Petzold, A., Prather, M. J., Schumann, U., Bais, A., Berntsen, T., Iachetti, D., Lim, L. L., and Sausen, R.: Transport impacts on atmosphere and climate: Aviation, Atmos. Environ., 44, 4678–4734, https://doi.org/10.1016/j.atmosenv.2009.06.005, 2010.

Lee, D. S., Fahey, D. W., Skowron, A., Allen, M. R., Burkhardt, U., Chen, Q., Doherty, S. J., Freeman, S., Forster, P. M., Fuglestvedt, J., Gettelman, A., De León, R. R., Lim, L. L., Lund, M. T., Millar, R. J., Owen, B., Penner, J. E., Pitari, G., Prather, M. J., et al.: The contribution of global aviation to anthropogenic climate forcing for 2000 to 2018, Atmos. Environ., 244, 117834, https://doi.org/10.1016/j.atmosenv.2020.117834, 2021.

Lefebvre, A. H. and Ballal, D. R.: Gas Turbine Combustion, CRC Press, Boca Raton, FL, https://doi.org/10.1201/9781420086058, 2010.

Liu, H., Tian, H., Hao, Y., Liu, S., Liu, X., Zhu, C., Wu, Y., Liu, W., Bai, X., and Wu, B.: Atmospheric emission inventory of multiple pollutants from civil aviation in China: Temporal trend, spatial distribution characteristics and emission features analysis, Sci. Total Environ., 648, 871–879, https://doi.org/10.1016/j.scitotenv.2018.07.407, 2019.

Lobo, P., Durdina, L., Brem, B. T., Crayford, A. P., Johnson, M. P., Smallwood, G. J., Siegerist, F., Williams, P. I., Black, E. A., Llamedo, A., Thomson, K. A., Trueblood, M. B., Yu, Z., Hagen, D. E., Whitefield, P. D., Miake-Lye, R. C., and Rindlisbacher, T.: Comparison of standardized sampling and measurement reference systems for aircraft engine non-volatile particulate matter emissions, J. Aerosol Sci., 145, 105557, https://doi.org/10.1016/j.jaerosci.2020.105557, 2020.

Lu, B., Dong, J., Wang, C., Sun, H., and Yao, H.: High-resolution spatio-temporal estimation of CO2 emissions from China's civil aviation industry, Appl. Energy, 373, 123907, https://doi.org/10.1016/j.apenergy.2024.123907, 2024.

Lu, B., Shi, L., Wang, C., Sun, H., Guo, Q., Wang, X., & Wang, X.:High-Resolution Gridded Aviation Emission Inventory for China (2023) [Data set]. Zenodo. https://doi.org/10.5281/zenodo.20828076, 2026.

Ma, S., Wang, X., Han, B., Zhao, J., Guan, Z., Wang, J., Zhang, Y., Liu, B., Yu, J., Feng, Y., and Hopke, P. K.: Exploring emission spatiotemporal pattern and potential reduction capacity in China's aviation sector: Flight trajectory optimization perspective, Sci. Total Environ., 951, 175558, https://doi.org/10.1016/j.scitotenv.2024.175558, 2024.

Ma, S., Lin, S., Han, B., Zhang, C., Wei, Z., Xue, L., Zhao, J., Wang, K., Yu, J., and Hopke, P. K.: Revealing considerable emissions reduction potential in flight operations: A real-time emission perspective, Transport. Res. D-Tr. E., 143, 104745, https://doi.org/10.1016/j.trd.2025.104745, 2025.

Nuic, A., Poles, D., and Mouillet, V.: BADA: An advanced aircraft performance model for present and future ATM systems, Int. J. Adapt. Control Signal Process., 24, 850–866, https://doi.org/10.1002/acs.1176, 2010.

Olsen, S. C., Wuebbles, D. J., and Owen, B.: Comparison of global 3-D aviation emissions datasets, Atmos. Chem. Phys., 13, 429–441, https://doi.org/10.5194/acp-13-429-2013, 2013.

Quadros, F. D. A., Snellen, M., Sun, J., and Dedoussi, I. C.: Global Civil Aviation Emissions Estimates for 2017–2020 Using ADS-B Data, J. Aircraft, 59, 1394–1405, https://doi.org/10.2514/1.C036763, 2022.

Schumann, U., Mayer, B., Graf, K., and Mannstein, H.: A Parametric Radiative Forcing Model for Contrail Cirrus, J. Appl. Meteorol. Climatol., 51, 1391–1406, https://doi.org/10.1175/JAMC-D-11-0242.1, 2012.

Schürmann, G., Schäfer, K., Jahn, C., Hoffmann, H., Bauerfeind, M., Fleuti, E., and Rappenglück, B.: The impact of NO_x, CO and VOC emissions on the air quality of Zurich airport, Atmos. Environ., 41, 103–118, https://doi.org/10.1016/j.atmosenv.2006.07.030, 2007.

Seymour, K., Held, M., Georges, G., and Boulouchos, K.: Fuel Estimation in Air Transportation: Modeling global fuel consumption for commercial aviation, Transport. Res. D-Tr. E., 88, 102528, https://doi.org/10.1016/j.trd.2020.102528, 2020.

Simaiakis, I. and Balakrishnan, H.: A Queuing Model of the Airport Departure Process, Transport. Sci., 50, 94–109, https://doi.org/10.1287/trsc.2015.0603, 2016.

Simone, N. W., Stettler, M. E. J., and Barrett, S. R. H.: Rapid estimation of global civil aviation emissions with uncertainty quantification, Transport. Res. D-Tr. E., 25, 33–41, https://doi.org/10.1016/j.trd.2013.07.001, 2013.

https://doi.org/10.5194/essd-2026-530
Preprint. Discussion started: 12 August 2026

Sobol, I. M.: Global sensitivity indices for nonlinear mathematical models and their Monte Carlo estimates, Math. Comput. Simulat., 55, 271–280, https://doi.org/10.1016/S0378-4754(00)00270-6, 2001.

Stettler, M. E. J., Boies, A. M., Petzold, A., and Barrett, S. R. H.: Global Civil Aviation Black Carbon Emissions, Environ. Sci. Technol., 47, 10397–10404, https://doi.org/10.1021/es401356v, 2013.

Teoh, R., Engberg, Z., Shapiro, M., Dray, L., and Stettler, M. E. J.: The high-resolution Global Aviation emissions Inventory based on ADS-B (GAIA) for 2019–2021, Atmos. Chem. Phys., 24, 725–744, https://doi.org/10.5194/acp-24-725-2024, 2024.

Tian, Y., He, X., Xu, Y., Wan, L., and Ye, B.: 4D Trajectory Optimization of Commercial Flight for Green Civil Aviation, IEEE Access, 8, 62815–62829, https://doi.org/10.1109/ACCESS.2020.2984488, 2020.

Unal, A., Hu, Y., Chang, M. E., Talat Odman, M., and Russell, A. G.: Airport related emissions and impacts on air quality: Application to the Atlanta International Airport, Atmos. Environ., 39, 5787–5798, https://doi.org/10.1016/j.atmosenv.2005.05.051, 2005.

Wang, J., Zu, L., Zhang, S., Jiang, H., Ni, H., Wang, Y., Zhang, H., and Ding, Y.: Recent Advances and Implications for Aviation Emission Inventory Compilation Methods, Sustainability, 16, 8507, https://doi.org/10.3390/su16198507, 2024.

Wang, L., Wu, C., and Sun, R.: An analysis of flight Quick Access Recorder (QAR) data and its applications in preventing landing incidents, Reliab. Eng. Syst. Safe., 127, 86–96, https://doi.org/10.1016/j.ress.2014.03.013, 2014.

Wang, Y., Li, H., Zheng, R., and Song, K.: Estimation of aircraft pollution emissions based on QAR data, in: 2023 International Conference on Computer Applications Technology (CCAT), Guangzhou, China, 196–200, https://doi.org/10.1109/CCAT59108.2023.00043, 2023.

Wasiuk, D. K., Lowenberg, M. H., and Shallcross, D. E.: An aircraft performance model implementation for the estimation of global and regional commercial aviation fuel burn and emissions, Transport. Res. D-Tr. E., 35, 142–159, https://doi.org/10.1016/j.trd.2014.11.022, 2015.

Wilkerson, J. T., Jacobson, M. Z., Malwitz, A., Balasubramanian, S., Wayson, R., Fleming, G., Naiman, A. D., and Lele, S. K.: Analysis of emission data from global commercial aviation: 2004 and 2006, Atmos. Chem. Phys., 10, 6391–6408, https://doi.org/10.5194/acp-10-6391-2010, 2010.

Woody, M., Haeng Baek, B., Adelman, Z., Omary, M., Fat Lam, Y., Jason West, J., and Arunachalam, S.: An assessment of Aviation's contribution to current and future fine particulate matter in the United States, Atmos. Environ., 45, 3424–3433, https://doi.org/10.1016/j.atmosenv.2011.03.041, 2011.

Xu, H., Xiao, K., Cheng, J., Yu, Y., Liu, Q., Pan, J., Chen, J., Chen, F., and Fu, Q.: Characterizing aircraft engine fuel and emission parameters of taxi phase for Shanghai Hongqiao International Airport with aircraft operational data, Sci. Total Environ., 720, 137431, https://doi.org/10.1016/j.scitotenv.2020.137431, 2020.

Yang, X., Cheng, S., Lang, J., Xu, R., and Lv, Z.: Characterization of aircraft emissions and air quality impacts of an international airport, J. Environ. Sci., 72, 198–207, https://doi.org/10.1016/j.jes.2018.01.007, 2018.

Yanto, J. and Liem, R. P.: Aircraft fuel burn performance study: A data-enhanced modeling approach, Transport. Res. D-Tr. E., 65, 574–595, https://doi.org/10.1016/j.trd.2018.09.014, 2018.

Yim, S. H. L., Lee, G. L., Lee, I. H., Allroggen, F., Ashok, A., Caiazzo, F., Eastham, S. D., Malina, R., and Barrett, S. R. H.: Global, regional and local health impacts of civil aviation emissions, Environ. Res. Lett., 10, 034001, https://doi.org/10.1088/1748-9326/10/3/034001, 2015.

Yim, S. H. L., Stettler, M. E. J., and Barrett, S. R. H.: Air quality and public health impacts of UK airports. Part II: Impacts and policy assessment, Atmos. Environ., 67, 184–192, https://doi.org/10.1016/j.atmosenv.2012.10.017, 2013.

Yoder, T. A.: Development of aircraft fuel burn modeling techniques with applications to global emissions modeling and assessment of the benefits of reduced vertical separation minimums, PhD Thesis, Massachusetts Institute of Technology, Cambridge, MA, USA, available at: https://dspace.mit.edu/handle/1721.1/39713, 2007.

Zhang, J., Zhang, S., Zhang, X., Wang, J., Wu, Y., and Hao, J.: Developing a High-Resolution Emission Inventory of China's Aviation Sector Using Real-World Flight Trajectory Data, Environ. Sci. Technol., 56, 5743–5752, https://doi.org/10.1021/acs.est.1c08741, 2022.

Zhang, X., Chen, X., and Wang, J.: A number-based inventory of size-resolved black carbon particle emissions by global civil aviation, Nat. Commun., 10, 534, https://doi.org/10.1038/s41467-019-08491-9, 2019.

Zhao, Y., Zhu, M., Zhou, L., Gao, M., Xu, Z., Zhong, S., Pan, K., and Chen, L.: Evaluating high-resolution aviation emissions using real-time flight data, Sci. Total Environ., 951, 175429, https://doi.org/10.1016/j.scitotenv.2024.175429, 2024.